A Study of the Liver-Heart Artifact in Emission Tomography

Johan Nuyts, Patrick Dupont, Vera Van den Maegdenbergh, Stefaan Vleugels, Paul Suetens, Luc Mortelmans

Department of Nuclear Medicine, Lab for Neuro-and Psychophysiology, ESAT-Machine Intelligence and Imaging, K.U. Leuven, Belgium

With the introduction of ^{99m}Tc-teboroxime, a previously undocumented artifact has shown up in cardiac SPECT imaging. In the images, the uptake values near the inferior wall are lower than expected. The artifact has been reported in the literature, but an adequate explanation has not yet been provided. The high uptake of ^{99m}Tc-teboroxime in the liver has been demonstrated to be the cause of this artifact. **Methods:** With simulations we show that an artifact can be reproduced by applying filtered backprojection (without corrections for attenuation) of attenuated and blurred projections. The conclusions from the simulations are validated with SPECT and PET phantom measurements. Maximum likelihood expectation maximization (ML-EM) reconstruction is applied to evaluate the effect of accurate attenuation correction. The influence of the high liver uptake on the convergence of ML-EM was also evaluated. **Results:** The artifact results mainly when the photon attenuation during reconstruction is ignored. This results in a distorted reconstruction of the liver. These distortions affect the neighboring inferior wall of the myocardium. While the use of opposite projections reduces the effect, accurate attenuation correction nearly eliminates it. A small additional deformation is caused by the position dependence of the spatial resolution of the gamma camera. It was also noted that the presence of the liver slows down the convergence of ML-EM in the heart region. **Conclusion:** The liver-heart artifact is an attenuation effect and is eliminated by attenuation correction. The local convergence of ML-EM is affected by the total image content.

Key Words: artifact; attenuation correction; teboroxime

In a recent publication (*1*), Germano et al. showed an artifact in a cardiac SPECT study with ^{99m}Tc-Teboroxime. The pixel values near the inferior wall of the left ventricle were abnormally low. With phantom measurements the authors showed that the artifact was caused by the high tracer uptake in the liver. However, no detailed explanation of the artifact was provided. Similar artifacts have been reported by Chua et al. and O'Conner et al. (*2,3*).

Several authors have studied how various unavoidable

physical effects which are ignored in the reconstruction may cause artifacts in the resulting SPECT images. Often correction algorithms are suggested as well. Such sources of artifacts are attenuation (*4–8*), position dependent resolution (*5–10*), Compton scatter (*4,6,11,12*), patient motion (*13*), organ motion (*14*) and tracer washout (*15*).

In this paper we focus on the artifacts caused by the presence of an object with very high tracer uptake. In Germano et al. (*1*), the authors show that negative pixel values are introduced by filtering projections with a ramp filter. These values are not completely canceled out in the subsequent backprojection step. Consequently, we hypothesize that the artifact is due to inconsistencies in the projections, since filtered backprojection (FBP) does not introduce significant negative values for consistent projections. The most obvious causes of inconsistencies in the reported phantom studies are photon attenuation and the position-dependent point spread function. We present the results obtained from simulation of SPECT acquisitions taking both of these effects into account. The results are verified with phantom measurements. Finally, the same phantom was measured with a PET-scanner to verify the effect of accurate attenuation correction and of a point spread function which is relatively stationary in comparison with SPECT.

MATERIALS AND METHODS

Simulations

We simulated two single-slice objects:

Object 1: A cylindrical background (radius 110 mm, attenuation 0.012 mm^{-1} [=attenuation of water], activity 28) and a ring-shaped object, representing the heart (inner radius 24 mm, thickness 9.6 mm, attenuation 0.012 mm^{-1}, activity 85). Activity is expressed in arbitrary units since the ratio between activity of object and background is the only important parameter. The size of the heart corresponds approximately to a normal human heart.

Object 2: Object 1 together with an irregular shaped object representing the liver (attenuation 0.012 mm^{-1}, activity 255). The smallest distance between the "liver" and the "heart" was 14.4 mm. The pixel size was 4.8 mm. The shape of the liver object was drawn to match that used in the phantom experiments described below (Fig. 1).
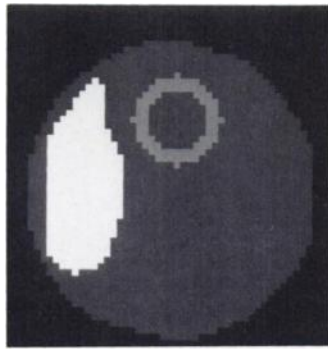
FIGURE 1. The simulated object representing high liver uptake close to the left ventricular wall.

TABLE 1
Dimensions and Radioactivity Levels of the Phantom Measured with the SPECT and PET Cameras

	Cylinder	Heart	Liver
Inner radius (mm)	108	18.5	—
Outer radius (mm)	111.5	30.0	—
Volume (ml)	6000	110	250
^{99m}Tc concentration [μCi/ml]	0.25	3.2	9.0
^{18}F concentration [μCi/ml]	0.15	2.0	5.0

Remark that Object 1 is in fact Object 2, but with a "liver" tracer uptake that is identical to that of the background. The attenuation of both objects is identical. In all simulations of 180° acquisitions, the camera started at the right, rotated in counter clockwise direction towards the top and further to its final position at the left (Fig. 2).

Four sets of projections over 180° have been calculated for Objects 1 and 2. The projections simulated correspond to the typical cardiac SPECT acquisition: the projections are acquired symmetrically around the angle where attenuation of the heart is minimal (left anterior in patients). The simulated camera is closest to the liver in the final projections. The first set of projections was not affected by attenuation and had an ideal point spread function (Dirac impulse). It was calculated by scanning a line through each of the projection pixels (step size 0.5 pixels). The second set of projections was calculated in a similar manner taking the attenuation into account. The third set of projections was affected by a position-dependent point spread function, modeling the blurring due to the collimator. This was simulated by applying a one-dimensional Gaussian convolution mask to the object prior to projection. The one-dimensional mask was perpendicular to the direction of projection. The standard deviation (in mm) of the Gaussian increased linearly with the distance d (in mm) to the collimator:

$$\sigma(d) = 1.7 + 0.023 * d. \qquad \text{Eq. 1}$$

This corresponds approximately to an intrinsic resolution of 4 mm FWHM and a resolution of 15 mm FWHM at a distance of 200 mm
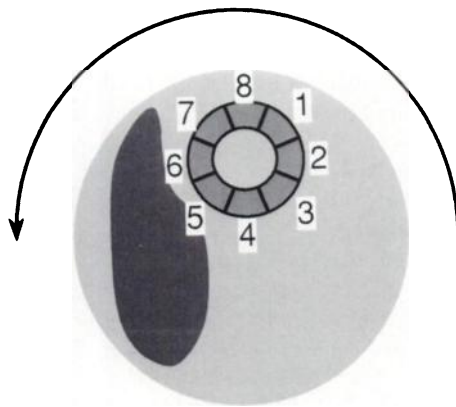

FIGURE 2. Eight regions drawn on the heart image. The arrow indicates the rotation angle in the case of 180° acquisition for both the simulations and the phantom measurements. For the 360° acquisition, this same arc is completed up to the starting position.

from the collimator. These characteristics are similar to those of the SPECT camera and collimator used for the phantom measurements. Finally, the fourth set of projections was affected by both attenuation and nonstationary point spread function.

These four sets were reconstructed with FBP, using a Hann filter (cutoff at the Nyquist frequency 0.104 cycles/cm), without any correction for attenuation or resolution effects. This approach is widely used in clinical cardiac SPECT. The whole procedure was repeated simulating a 360° acquisition.

In order to assess the effect of the liver to heart distance on the artifact, different versions of Object 2 (with projections affected by point spread function and attenuation) were produced by shifting the liver horizontally, thus obtaining distances of 0 to 5 pixels or 0 to 24 mm. Similarly, the activity level of the liver was changed in order to evaluate the influence of the liver to heart activity ratio. Simulations were performed for a liver to heart ratio of activity of 0.3 (i.e., liver activity equal to background), 0.7, 1, 2 and 3.

Comparing the results of Objects 1 and 2, we can evaluate the influence of the high liver uptake.

Phantom Measurements

A phantom experiment similar to the simulated object has been performed. Two objects were mounted in a perspex cylinder: a cardiac phantom and a plastic perfusion bag, secured by tape to ensure it did not move. The wall of the cardiac phantom was filled with a homogeneous solution of ^{99m}Tc in water, the blood pool with cold water. A water filled perfusion bag was used to simulate the liver. The ^{99m}Tc concentration in the bag was approximately three times higher than in the heart phantom. The cylinder was filled with a low concentration of ^{99m}Tc in water. The dimensions and radioactivity levels are listed in Table 1.

The phantom was placed on the patient bed of a gamma camera. Sixty-four projections over 360° were acquired, using a 64 × 64 projection matrix (pixel size 4.8 mm). The acquisition duration was 60 sec per projection. The first 32 projections corresponded to those of a typical cardiac SPECT study. They were extracted to be reconstructed with FBP without correction for attenuation or resolution effects. The entire set of 64 projections was also reconstructed with FBP.

Several days later, the phantom was filled with ^{18}F-altanserine (available from a previous study) for measurement in the PET. The activity concentrations are given in Table 1. The camera acquired 15 sinograms, consisting of 256 projections with 192 pixels per projection. A study of 1 hr was acquired. After 8.5 half-lives decay of ^{18}F a 30 min transmission scan was performed (570 million counts). A blank scan of 30 min (760 million counts) was acquired before the emission scan. The sinograms were normalized, corrected for attenuation and reconstructed with FBP.
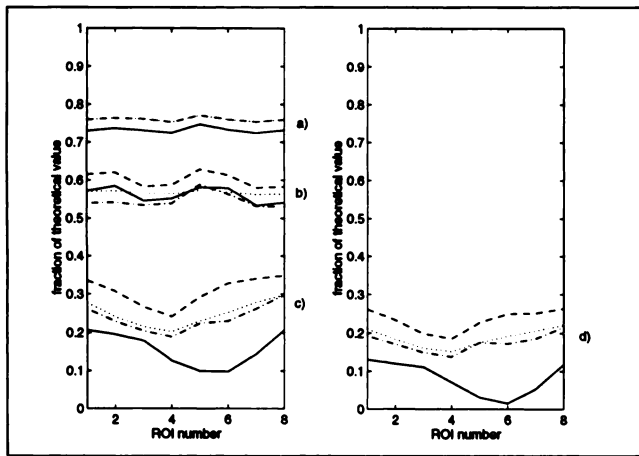
FIGURE 3. Plot of the mean value in each of the myocardial regions as fraction of the theoretical value. The regions are applied to the filtered backprojection of the simulated Objects 1 (only heart) and 2 (heart and liver) in (a) the ideal case, (b) in the case of projections affected by a nonstationary point spread function, (c) by attenuation and (d) by both attenuation and a nonstationary point spread function.   Heart image, 180°: ––; Heart image, 360°: ····; Heart/liver, 180°: —; Heart/liver, 360°: ––.   In the ideal case, the curves for 180° and 360° coincide for both of the objects.

FIGURE 5. The relative error caused by the liver-heart artifact, as a function of the liver to heart activity ratio. The error is defined as zero when the activity in the liver equals that of the background. The projections were affected by attenuation and position-dependent blurring. Only the regions in which the artifacts were least pronounced (region 3) and most severe (region 6) are shown. (∗ = 180°, O = 360°).

Iterative Reconstruction

In order to correct the SPECT phantom images for attenuation, transmission maps were derived from the reconstructed images. Since the cylinder was filled with a small concentration of ^{99m}Tc, the border of the attenuating object can be traced in the emission images. A region was drawn along the border of the cylinder in two slices, in order to determine the center coordinates in these slices. Because the axis of the cylinder was almost parallel to the rotation axis of the SPECT camera, we assumed a cylindrical cross section in every slice. Knowing the diameter of the cylinder, the position of its axis in two slices and the effective attenuation coefficient (0.012 mm^{-1}), we could calculate an attenuation map for every slice.
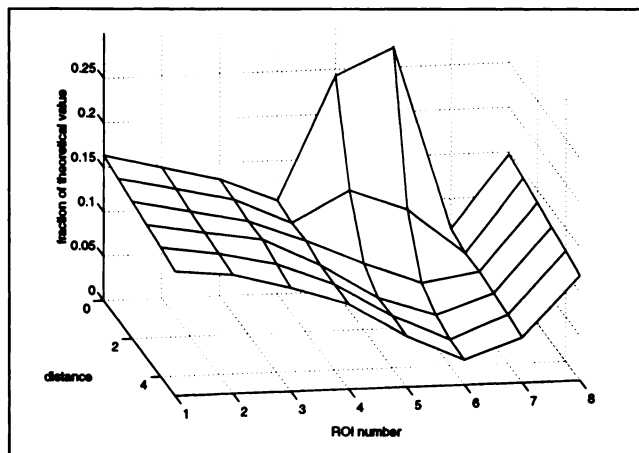

FIGURE 4. The mean (relative) value in each of the myocardial regions for the filtered backprojection of the 180° simulation, as a function of the distance between the heart and the liver. The distance is increased from 0 to 5 pixels (4.8 mm per pixel). The projections were affected by attenuation and position-dependent blurring.
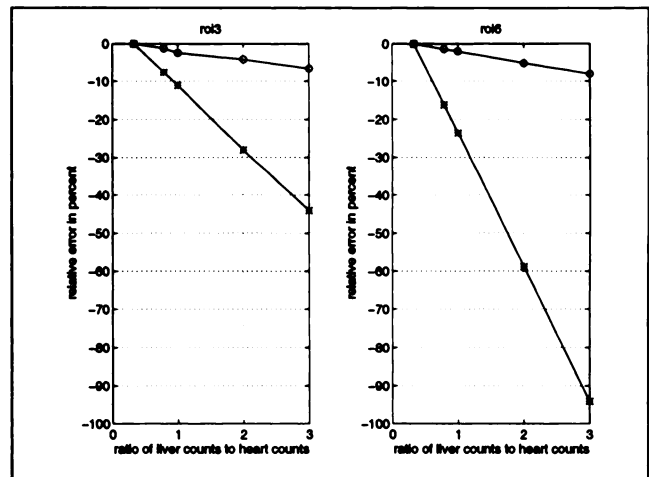
Using the calculated attenuation map and the measured projections, 60 iterations of ML-EM reconstruction algorithm (16,17) were applied to both the 180° and the 360° acquisitions. The resulting reconstructions are accurately corrected for attenuation, but no correction for the position-dependent point spread function was included.

To evaluate the influence of the high liver uptake on the convergence of ML-EM, 20, 60 and 100 ML-EM iterations were calculated for projections of Objects 1 (heart-like object without liver activity) and 2 (same object combined with liver activity). In these tests attenuation was set to zero and no point spread function was simulated. The simulated acquisition over 180° was used.

Polar Maps

Polar maps represent the tracer uptake in the left ventricle of the heart in a simple two-dimensional image, which is suited for visual or quantitative analysis (18). This approach is often used in cardiac applications. For the current application, polar maps show the effect of the artifact to the tracer uptake values for the entire left ventricle in a single image. For these reasons, we have processed the reconstructed phantom images with our cardiac analysis software (19) to generate the corresponding polar maps.

RESULTS

The eight sets of projections (of Objects 1 and 2) have been reconstructed with FBP, without correction for attenuation or point spread function. Eight regions were drawn on the heart in all the images of Objects 1 and 2 (Fig. 2). In all regions the mean value was calculated (Fig. 3). In reconstruction from attenuated projections, the high liver uptake causes an additional decrease of up to 20% of the true value in heart regions close to the liver. Note that for the ideal projections, the reconstructed value was lower than the true value, because of smoothing by the Hann reconstruction filter.

FIGURE 6. Reconstruction of simulated projections over 180°, taking into account both attenuation and point spread function: filtered backprojection (left), ML-EM (center) and ML-EM with attenuation compensation (right).
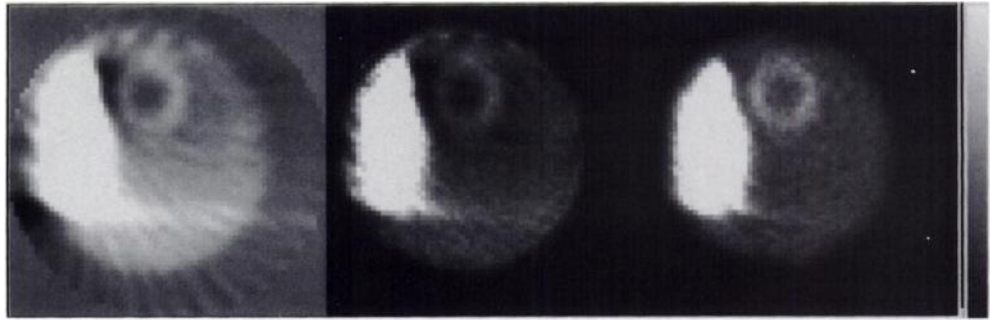
Figure 4 shows the influence of the liver to heart distance. At very small distances, collimator blurring dominates and activity from the liver spills over into the myocardium (regions 5–7). As the distance increases, the spillover reduces and the artifact becomes dominant.

Figure 5 shows the severity of the liver-heart artifact as a function of the liver to heart activity ratio. For 180° acquisitions the artifacts can be very prominent. Using opposite projections results in strong suppression of the artifact.

In Figure 6 the reconstruction of the simulated heart-liver object is shown for a 180° acquisition with projections affected by attenuation and a nonstationary point spread function. In order to clearly show the pixel values in the heart region, the values in the liver were clipped to a value about 3 times smaller than the image maximum. For FBP (left) the liver is surrounded by negative values which also decrease the count rate in the heart region. The nonstationary point spread function further degrades the image. ML-EM reconstruction without attenuation correction (center) shows a strong reduction of the artifact, and ML-EM with attenuation correction nearly eliminates it (right). Figure 7 shows the FBP of the measured phantom projections for the 180° and the 360° acquisitions, and the ML-EM reconstruction of the 360° acquisition. The artifacts in FBP (of the 180° acquisition, Fig. 7, left), are similar to those seen in the simulations (Fig. 6, left). In both images the liver is severely deformed: negative counts show up between liver and heart and at the opposite edge of the liver. Positive streaks appear near the lower right portion of the liver. The inclusion of the opposing projections (360° acquisition) reduces the artifacts (Fig. 7, center). Attenuation correction by ML-EM eliminates the artifact (Fig. 7, right).

Figure 8 shows the polar maps of the phantom measurements for acquisitions of both 180° and 360° and for reconstructions with FBP and ML-EM with and without attenuation correction. The polar map of the PET phantom is also shown. The artifact is most prominent in the 180° SPECT acquisition, reconstructed with FBP. The use of all 64 projections reduces the effect, although it still is unacceptable for clinical practice. Iterative reconstruction without attenuation compensation is clearly superior to FBP for both 180 and 360°. Accurate attenuation correction nearly eliminates the effect. The PET polar map is almost homogeneous. The quantitative analysis with the eight regions of Figure 2 confirms these results (Fig. 9).

Figure 10 presents the effect of the high liver activity on the convergence of ML-EM reconstruction as revealed by the simulations. In the absence of the liver, the difference between the 60th and 100th ML-EM reconstructions is small, and both are close to ideal. In the presence of the liver, the corresponding iterations do not show the same level of convergence.

DISCUSSION

The term "attenuation artifact" is only meaningful when attenuation is ignored in the reconstruction. FBP is most widely used in clinical practice and in most cases no attenuation correction is applied. The "artifact" attributed most to attenuation is that of local underestimation of the actual tracer uptake. The degree of underestimation is usually assumed to be proportional to the average attenuation over

FIGURE 7. Technetium-99m phantom. Filtered backprojection of a slice from the phantom SPECT acquisition over 180° (left) and 360° (center), and the ML-EM reconstruction (360° acquisition and attenuation compensation) of the same slice (right).
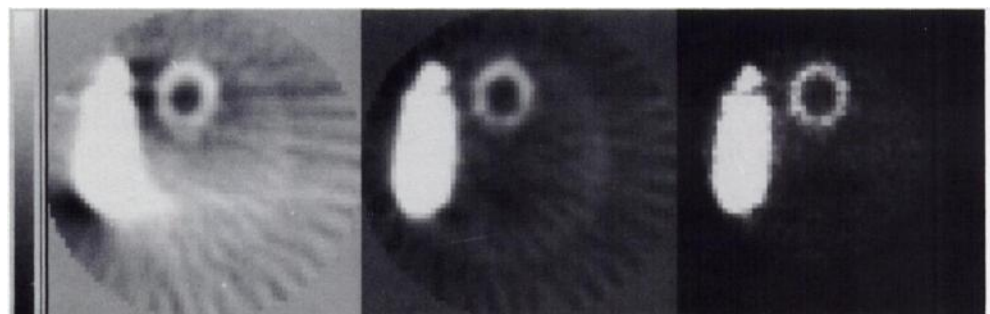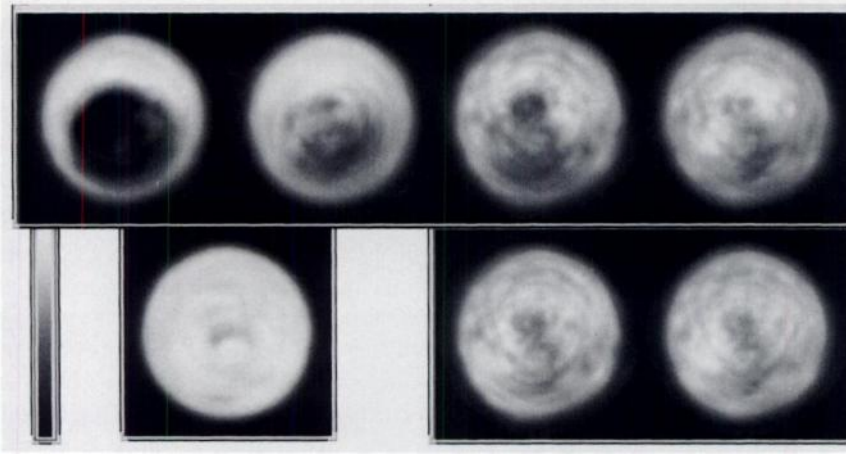
FIGURE 8. Polar maps derived from the phantom SPECT and PET measurements. Top row, from left to right: filtered backprojection (FBP), 180°; FBP 360°; ML-EM 60 iterations, 180°; ML-EM 60 iterations, 360°. Bottom row, from left to right: polar map derived from the PET measurement using FBP; ML-EM 60 iterations, 180°, attenuation correction; ML-EM 60 iterations, 360°, attenuation correction.

all projections. This assumption has led to the well-known multiplicative attenuation correction algorithm of Chang (20). The assumption is acceptable in relatively symmetrical cases, i.e., when the attenuation in the different projections is in the same order. In asymmetric cases, however, attenuation causes strong inconsistencies in the projections. This means that no realistic object that would produce such a set of projections in absence of attenuation exists. Since FBP assumes absence of attenuation, there is no solution. FBP, however, always generates a reconstruction image, by backprojecting the filtered projections. In consistent projections the negative values introduced by the filter cancel out the positive values from the backprojection blurring. In inconsistent projections, this is not exactly the case. This results in residual negative values from the filter and streak artifacts from the backprojection. Similar but less severe inconsistencies are introduced by the nonstationary point spread function. In structures which are blurred differently in different projections, these inconsistencies will again produce negative values and streaks in the reconstruction. These artifacts have been described
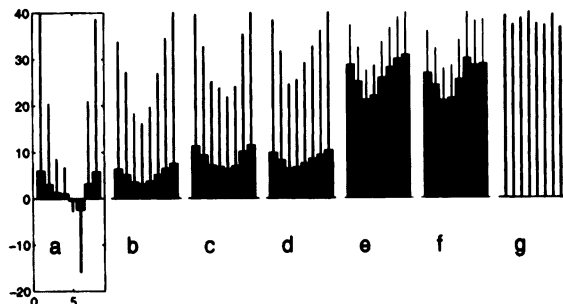
previously using simulations and phantom studies by Eisner et al. (5).

In 360° acquisition opposing projections are added. This reduces the difference in blurring and attenuation between the different projections therefore reducing the reconstruction artifacts.

From the previous considerations it is obvious that the severity of artifact increases with increasing liver uptake. The artifact is strongest in 180° acquisitions with projections influenced by both attenuation and a nonstationary point spread function (Fig. 3).

The simulations and phantom measurements show that attenuation deforms the FBP reconstruction of the liver in such a way that negative counts are introduced (Figs. 6 and 7). FBP is linear—the reconstruction of an attenuated heart image may be added to the reconstruction of an attenuated liver image to obtain the final image. The artifact due to the
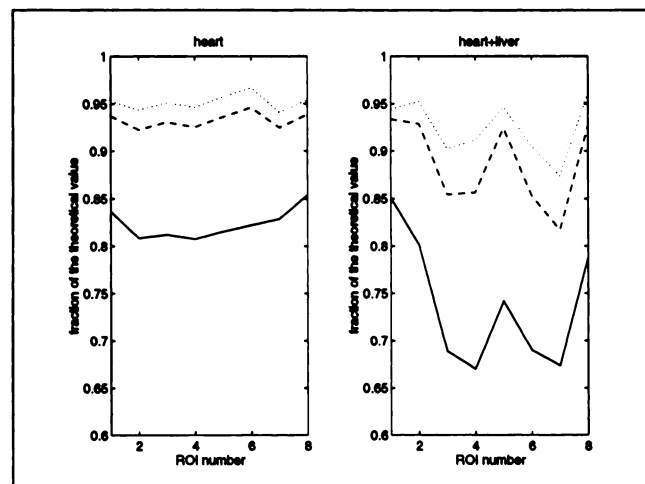

FIGURE 9. Plots of the mean values in eight regions drawn on the reconstructions of the phantom studies. The regions were similar to the ones used for the simulation. Thick bars represent the actual reconstruction values, thin bars represent the same values after normalization to the maximum value of the eight regions. (a) FBP 180°, (b) FBP 360°, (c) ML 180°, (d) ML 360°, (e) ML 180°, attenuation correction, (f) ML 360°, attenuation correction, (g) FBP PET.

FIGURE 10. Plot of the mean value in each of the myocardial regions as a fraction of the theoretical value. The regions are applied to the ML-EM reconstructions of the heart (Object 1) and of the liver-heart (Object 2) projections for 20, 60 and 100 iterations. These projections were calculated ignoring attenuation and point spread function. ML-EM 20 iterations: —; ML-EM 60 iterations: ––; ML-EM 100 iterations: ·····.

liver is simply added to the reconstructed heart image. It follows that the artifact observed in the heart is proportional to the ratio of liver count rate to heart count rate, which is confirmed by our simulations (Fig. 5). Increasing the symmetry by using projections over 360° reduces the artifact considerably (Fig. 5). Also, the distance between the liver and heart has a strong effect on the severity and features of the artifact (Fig. 4). Consequently, the artifact is likely to be very patient-dependent and its severity is hard to predict.

Figures 8 and 9 show that accurate attenuation correction by ML-EM virtually eliminates the effect. The reconstructions are still not perfectly homogeneous probably mainly due to position-dependent blurring. Additional errors may be caused by possible deviations between the assumed and actual attenuation coefficients and by alignment errors between the artificial attenuation map and the emission image. The ML-EM reconstruction of the 360° acquisition seems slightly superior to that of the 180°. Most likely, the effects of the nonstationary point spread function are reduced by the use of the opposite projections. Our current software did not allow us to verify whether inclusion of the nonstationary point spread function would significantly improve the ML-EM reconstructions. In PET, the point spread function is fairly uniform and the transmission and emission images well aligned. The resulting profile and polar map are uniform.

Figure 3 clearly shows that without the presence of the liver, the image of the heart is severely affected by photon attenuation. The hot liver artifact causes only a further degradation of the image.

It is interesting to see that the ML-EM reconstructions without attenuation correction are clearly superior to the FBP-images. ML-EM automatically suppresses the artifact by its inherent non-negativity constraint. In addition, unlike FBP, it assigns different weights to the projection values. As a result, the value of a pixel is less affected by projection values which suffered strongest attenuation. It is likely that this weighting further reduces the influence of inconsistencies due to attenuation.

The straightforward approach for eliminating the hot liver artifact is accurate attenuation correction, e.g., with ML-EM reconstruction. This is only possible when an attenuation map is available. Several researchers are investigating hardware and software tools that will enable transmission tomography on SPECT cameras in clinical practice (21–24).

Finally, Figure 10 issues a warning: the local convergence of ML-EM depends on the total image content. High tracer uptake in the liver significantly slows down convergence of the heart region. If the image noise produced in the higher ML-EM iterations is suppressed by applying stopping rules (25) or cross-validation techniques (26), it may be useful to verify that stopping the iterations does not produce artifactual decreases in the activity of the wall. Of course, attenuation correction will only suppress artifacts caused by the mere presence of a constant high activity

near the object of interest. In clinical ^{99m}Tc-teboroxime studies, additional artifacts are caused by variations in the tracer concentration during acquisition (15).

CONCLUSION

High liver uptake typical in ^{99m}Tc-Teboroxime studies causes an artifactual decrease in the left ventricular wall count rate in FBP reconstructions. This artifact has been studied with simulations and phantom measurements. It is concluded that the main cause is the lack of attenuation correction. The inconstancy of the point spread function causes a smaller additional degradation of the image. Accurate attenuation correction with the maximum likelihood expectation maximization algorithm was shown to be effective in suppressing the artifact. Simulations showed that the presence of the hot liver has an adverse effect on the convergence of ML-EM in the heart region.

ACKNOWLEDGMENT

REFERENCES

1. Germano G, Chua T, Areeda J, Kiat H, Berman D. Hepatic uptake creates artifactual defects in ^{99m}Tc myocardial SPECT images: a quantitative phantom analysis. J Nucl Med 1994;35:356–359.
2. Chua T, Kiat H, Germano G, et al. Rapid back to back adenosine stress/rest Tc-99m teboroxime myocardial perfusion SPECT using a triple-detector camera. J Nucl Med 1993;34:1485–1493.
3. O'Conner MK, and Kelly BJ. Evaluation of techniques for elimination of hot bladder artifacts in SPECT of the pelvis. J Nucl Med 1990;31:1872–1875.
4. Chang W, Henkin RE, Buddemeyer E. The sources of overestimation in the quantification by SPECT of uptakes in a myocardial phantom: concise communication. J Nucl Med 1984;25:788–791.
5. Eisner RL, Nowak DJ, Fajman W. Fundamentals of 180° acquisition and reconstruction in SPECT imaging. J Nucl Med 1986;27:1717–1728.
6. Floyd CE, Jaszczak RJ, Greer KL, Coleman RE. Inverse Monte Carlo as a unified reconstruction algorithm for ECT. J Nucl Med 1986;27:1577–1585.
7. Knešaurek K, King MA, Glick SJ, Penney BC. Investigation of causes of geometric distortion in 180° and 360° angular sampling in SPECT. J Nucl Med 1989;30:1666–1675.
8. Van Elmbt L, Walrand S. Simultaneous correction of attenuation and distance dependent resolution in SPECT: an analytical approach. Phys Med Biol 1993;38:1207–1217.
9. Todd-Pokropek A. Nonstationary deconvolution using a multi-resolution stack. IPMI, 1988:277–289.
10. Lewitt RM, Edholm PR, Xia W. Fourier method for correction of depth-dependent collimator blurring. SPIE Vol 1092 Medical Imaging III: Image Processing, 1989;232–243.
11. Jaszczak RJ, Floyd CE Jr, Coleman RE. Scatter compensation techniques for SPECT. IEEE Trans Nucl Sci 1985;NS-32:786–793.
12. Ljunberg M, King MA, Hademenos GJ, Strand SV. Comparison of four scatter correction methods using Monte Carlo simulated source distributions. J Nucl Med 1994;35:143–151.
13. Eisner R, Churchwell A, Noever T, et al. Quantitative analysis of the tomographic thallium-201 myocardial bullseye display: critical role of correcting for patient motion. J Nucl Med 1988;29:91–97.
14. Friedman J, Van Train K, Maddahi J, et al. "Upward creep" of the heart: a frequent source of false-positive reversible defects during thallium-201 stress-redistribution SPECT. J Nucl Med 1989;30:1718–1722.
15. Nakajima K, Shuke N, Taki J, et al. A simulation of dynamic SPECT using radiopharmaceuticals with rapid clearance. J Nucl Med 1992;33:1200–1206.
16. Shepp LA, Vardi Y, Ra JB, Hilal SK, Cho ZH. Maximum likelihood reconstruction for emission tomography. IEEE Trans Med Imaging 1982; MI-1:113–122.
17. Lange K, Carson R. EM reconstruction algorithm for emission and transmission tomography. J Comput Assist Tomog 1984;MI-5:306–316.

18. Garcia EV, Van Train K, Maddahi J, et al. Quantification of rotational thallium-201 myocardial tomography. *J Nucl Med* 1985;26:17–26.

19. Nuyts J, Suetens P, Oosterlinck A, De Roo M, Mortelmans L. Delineation of ECT images using global constraints and dynamic programming. *IEEE Trans Med Imaging* 1991;MI-10:489–498.

20. Chang LT. A method for attenuation correction in radionuclide computed tomography. *IEEE Trans Nucl Sci* 1978;NS-25:638–643.

21. Bailey DL, Hutton BF, Walker PJ. Improved SPECT using simultaneous emission and transmission tomography. *J Nucl Med* 1987;28:844–851.

22. Manglos S, Gagne G, Bassano D. Quantitative analysis of image truncation in focal-beam CT. *Phys Med Biol* 1993;38:1443–1457.

23. Jaszczak R, Gilland DR, Hanson MW, Jang S, Greer KL, Coleman RE. Fast transmission CT for determining attenuation maps using a collimated line source, rotatable air-copper-lead attenuators and fan-beam collimation. *J Nucl Med* 1993;34:1577–1586.

24. Zeng GL, Gullberg GT, Jaszczak RJ, Li J. Fan-beam reconstruction algorithm for a spatially varying focal length collimator. *IEEE Trans Med Imaging* 1994;12:575–582.

25. Veklerov E, Llacer J. Stopping rule for the MLE algorithm based on statistical hypothesis testing. *IEEE Trans Med Imaging* 1987;MI-6:313–319.

26. Llacer J, Veklerov E, Coakley KJ, Hoffman EJ, Nunez J. Statistical analysis of maximum likelihood estimator images of human brain FDG-PET studies. *IEEE Trans Med Imaging* 1993;12:215–231.